Nitrogen solubility in basaltic silicate melt - Implications for degassing processes

Fabien Bernadou, Fabrice Gaillard, Evelyn Füri, Yves Marrocchi, Aneta
Slodczyk

Journal Pre-proof

Nitrogen solubility in basaltic silicate melt - Implications for degassing processes

Fabien Bernadou, Fabrice Gaillard, Evelyn Füri, Yves Marrocchi, Aneta Slodczyk
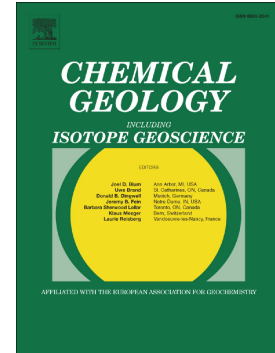
Please cite this article as: F. Bernadou, F. Gaillard, E. Füri, et al., Nitrogen solubility in basaltic silicate melt - Implications for degassing processes, *Chemical Geology* (2021), https://doi.org/10.1016/j.chemgeo.2021.120192

Chemical geology

Manuscript draft

Title: Nitrogen solubility in basaltic silicate melt - Implications for degassing processes

Article Type: Research paper

Keywords: Nitrogen, Solubility, oxygen fugacity, IHPV, SIMS

Abstract: The distribution of nitrogen between the different terrestrial reservoirs (core-mantle-atmosphere) and how this may have changed from the earliest planetary stages is uncertain. In particular, the primordial degassing processes of the magma ocean and its role in the formation of the atmosphere remains to be quantified. Since no geological samples can capture this early degassing process, we need to go through the thermodynamic modelling of the nitrogen solubility in silicate melt. We hence performed experiments on basaltic samples at fluid saturation in the C-H-O-N system, using an Internally Heated Pressure Vessel (IHPV) and Piston Cylinder (PC) in the pressure range 0.8 kbar to 10 kbar, temperature between 1200 and 1300°C, and a wide range of fO_2 conditions from IW+4.9 to IW-4.7 (Iron-Wustite redox buffer). The nitrogen concentration in the quenched silicate melts at fluid saturation was analysed by secondary ion mass spectrometry (SIMS), and the speciation of the dissolved C-O-H species was determined by Fourier transform infrared spectroscopy (FTIR). We identified two nitrogen species in the silicate melt: N_2 dominating at $fO_2 >$ IW and N^{3-} at lower fO_2. Using these data and a database constraining nitrogen concentration at fluid saturation from 1 bar to 10 kbar pressure, we calibrated a solubility law for nitrogen in basalts defining its P-T-fO_2 dependences. This model expands the model of Libourel et al. (2003) to high pressure and higher C-O-H activities. It can be used to investigate the nitrogen degassing processes for different pressure, temperature and fO_2 conditions relevant to planetary accretion and modern volcanism.

Nitrogen solubility in basaltic silicate melt - Implications for degassing processes

Fabien Bernadou *,[1], Fabrice Gaillard [1], Evelyn Füri [2], Yves Marrocchi [2], Aneta Slodczyk [1]

[1] : Institut des Sciences de la Terre d'Orléans, CNRS/Université d'Orléans/BRGM, 1a rue de la Férollerie 45071, Orléans cedex 2, France

[2] : Université de Lorraine, CNRS, CRPG, F-54000 Nancy, France

*: Corresponding author e-mail address: fabien.bernadou@cnrs-orleans.fr

Abstract

The distribution of nitrogen between the different terrestrial reservoirs (core-mantle-atmosphere) and how this may have changed since the earliest planetary stages is uncertain. In particular, the primordial degassing processes of the magma ocean and its role in the formation of the atmosphere remains to be quantified. Since no geological samples can capture this early degassing process, we need to go through the thermodynamic modelling of the nitrogen solubility in silicate melt. We hence performed experiments on basaltic samples at fluid saturation in the C-H-O-N system, using an Internally Heated Pressure Vessel (IHPV) and Piston Cylinder (PC) in the pressure range 0.8 kbar to 10 kbar, temperature between 1200 and 1300°C, and a wide range of fO$_2$ conditions from IW+4.9 to IW-4.7 (IW standing for the Iron-Wustite redox buffer). The nitrogen concentration in the quenched silicate melts at fluid saturation was analysed by secondary ion mass spectrometry

(SIMS), and the speciation of the dissolved C-O-H species was determined by Fourier transform infrared spectroscopy (FTIR). We identified two nitrogen species in the silicate melt: N_2 dominating at $fO_2 >$ IW and N^{3-} at lower fO_2. Using these data and a database constraining nitrogen concentration at fluid saturation from 1 bar to 10 kbar pressure, we calibrated a solubility law for nitrogen in basalts defining its P-T-fO_2 dependences. This model expands the model of Libourel et al. (2003) to high pressure and higher C-O-H activities. It can be used to investigate the nitrogen degassing processes for different pressure, temperature and fO_2 conditions relevant to planetary accretion and modern volcanism.

Key Words: Nitrogen, solubility, degassing, oxygen fugacity, IHPV, SIMS

1. Introduction

Whereas other volatile components such as H_2O or CO_2 have been intensively studied, there is a lack of information and comprehension on the nitrogen (N) behaviour in Earth's interior during the various stages of its formation. Nitrogen, however, dominates the current Earth's atmosphere and its availability for life molecules like amino acids -as highlighted by the experiment of Miller and Urey (Miller, 1953)- is probably an important prerequisite for habitability (Catling and Zahnle, 2020). Earth's nitrogen shows isotopic compositions close to those of enstatite chondrites, suggesting it was probably delivered during the main accretion stage (Marty, 2012). N must have been subsequently processed through the magma ocean stage and then possibly released via planetary magmatism during

the Hadean and Archean eons. Understanding the timing of nitrogen degassing is of primordial importance to capture the evolution of Earth's atmosphere (Zahnle et al., 2010). Although N_2 partial pressure and isotopic composition of the Archean atmosphere have been reported based on N analyses of fluid inclusions trapped in quartz (Marty et al., 2013), the N behaviour during the magma ocean and earliest terrestrial volcanism stages is still underconstrained.

According to the literature, the degassing of nitrogen from a silicate melt is enhanced by oxidizing conditions (Libourel et al., 2003; Boulliung et al., 2020). On the other hand, several recent studies of mantle-core differentiation (Dalou et al., 2017; Speelmanns et al., 2019) have highlighted that nitrogen can be moderately siderophile at oxygen fugacity closed to Iron-Wüstite redox buffer (IW-2), while it is magmatophile (ie. High affinity for the silicate melt phase) under more reduced conditions. This implies that from the most reduced to the most oxidizing conditions nitrogen behaviour must evolve from magmatophile to siderophile and then atmophile. Given this great diversity of possible N behaviour, tight and precise experimental constraints are needed to decipher the fate of nitrogen during these earliest differentiation events.

N solubility has been experimentally investigated in minerals (Li et al., 2013; Yoshioka et al., 2018) as well as silicate melts, fluids and metal alloys (Dalou et al., 2017; Kadik et al., 2015; Roskosz et al., 2013; Speelmanns et al., 2018, 2019; Grewal et al., 2019; Dalou et al., 2019a; Mosenfelder et al., 2019). In theory, all these data could be combined to address N magmatic degassing processes using thermodynamic modelling. Gaillard and Scaillet (2014) used the solubility model of Libourel et al. (2003) to predict degassing in the C-H-O-N-S

system, but no experimental verification of the validity of this model at pressure superior then 1 bar and in H-bearing system exists. In this study, we thus focus on magmatic nitrogen in order to capture the fluid-melt equilibria governing nitrogen degassing at medium pressure (0.8 to 2.4 kbar) and medium temperature (1200 to 1300°C).

According to Libourel et al. (2003), the nitrogen speciation in silicate melt can be split in two domains. For fO_2 more oxidizing than the Iron-Wüstite (IW) redox buffer, nitrogen is physically dissolved in the silicate melt and its concentration depends mainly on pressure (i.e., nitrogen partial pressure). Under these conditions N_2 (N^0 valence) is the dominant nitrogen species and its concentration in the silicate melt is usually low (i.e., << 100 ppm; Libourel et al., 2003). For oxygen fugacity more reduced than the IW redox buffer, nitrogen is chemically dissolved in the silicate melt; its concentration is high (>>100 ppm) and strongly correlated with fO_2 variations. The dominant chemically dissolved species is described as N^{3-} in a hydrogen free system (Libourel et al., 2003), while NH_3 species (N^{3-} valence) have been identified in H-bearing system (Kadik et al., 2015; Dalou et al., 2019b; Grewal et al., 2020; Mosenfelder et al., 2019) at high pressure. Some other minor species have been suggested such as CN^- (Dalou et al., 2019b) or NO^- (Roskosz et al., 2006). Therefore, in addition to N^{3-}, the potential role of CN^-, NO^- or NH_3 species in the solubility of nitrogen in basaltic system must be determined.

Considering the fluid phases at high pressure and high temperature, the nitrogen speciation in a N-H-O system mainly involves N_2 and NH_3 (Chen et al., 2019; Li and Keppler, 2014). The ratio between these two species depends on various parameters such as pressure, temperature, fO_2 and total nitrogen concentration in the fluid (Chen et al., 2019; Li

and Keppler, 2014). However, these studies report contrasting results, likely due to the different techniques used for characterizing the samples (in situ vs. post-mortem). According to Chen et al. (2019), it appears that post-mortem studies tend to overestimate the NH_3 stability domain, implying that at most magmatic conditions (low P, high T), N_2 should be the major N-species in the fluid (e.g P<5 kbar and T>1000°C).

Currently, the study by Libourel et al., 2003 remains the reference when it comes to modeling the behavior of nitrogen between silicate melt and fluid phase as it links nitrogen fugacity in the fluid to N contents in the silicate melt. However, this model uses low pressure data (i.e. 1 atm) in a H-free system. The study by Li et al., 2015 at medium pressure (i.e.> 1kbar) is interesting because it provides data on N solubility in H-bearing systems but their interpretatation being based on empirical fluid-melt partition coefficient, prevents a link with N fugacity and does not permit of Libourel et al. (2003) solubility model. There therefore remains a large shadow area concerning the medium and high pressure modeling.

In this study, we investigate nitrogen solubility in basaltic silicate melt, i.e., the nitrogen content in the quenched silicate melt at fluid saturation. We performed a series of experiments at intermediate pressure (0.8 to 10 kbar), high temperature (1200°C and 1300°C) and over a wide range of fO_2 (IW-4.72 to IW+4.91) in the C-H-O-N system with a starting material of basaltic composition. By combining our results and the available literature data, we calibrate a nitrogen solubility model operating from surficial to upper mantle conditions.

2. Experimental and analytical techniques

2.1. Starting material

The starting product is a natural basalt of Monte Sagnolo (Etna, Sicily; Gennaro et al., 2019). The basalt was crushed in an agate mortar with ethanol. The obtained powder was melted at 1 bar and 1400°C for 1 hour in a Pt crucible. The obtained glass was crushed and melted a second time in order to get a homogenous chemical composition. After a last fine crushing, the powders were stored away from moisture at 120°C in a stove. Nitrogen was added using different sources in the experimental charges (Table 1). aqueous solution of ammonia (NH_3 32%), nitric acid (HNO_3 65%) and dry powder of silicon (Si_3N_4) and iron nitride (Fe_xN) were used. The exact stoichiometry of the iron nitride was not provided by the supplier, a range between Fe_2N and Fe_4N is indicated. We conducted X-Ray Diffraction (XRD) and elemental analyser analysis indicating an average stoichiometry of $Fe_{3,5}N$. For the experimental charges where nitrogen was added as aqueous solution, we added graphite in order to dehydrate and buffer the carbon activity in the charges following the equilibria:

$$H_2O + C = H_2 + CO \tag{1}$$

$$2H_2O + C = 2H_2 + CO_2 \tag{2}$$

For the charges where we added nitrogen as solids, we used two nitride powders. Si_3N_4 was used as reducing agent (Dalou et al., 2017) following the reaction:

$$Si_3N_4 + 3O_2 \rightarrow 3SiO_2 + 2N_2 \tag{3}$$

In our cases the reaction involves the following components (Dalou et al., 2017):

$$6FeO + Si_3N_4 \rightarrow 6Fe + 3SiO_2 + 2N_2 \tag{4}$$
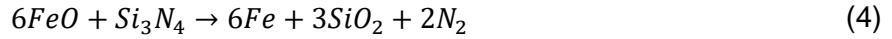
This resulted in glasses being depleted in FeO, enriched in SiO_2 and forming Fe metal alloys.

2.2. Experimental techniques

Samples were loaded in AuPd and Pt capsules. The various nitrogen sources were mixed with the basalt powders and graphite for the charges with aqueous solution. Palladium and iridium powders were also mixed with the starting products to create Fe-Pd and Fe-Ir alloys as fO_2 sensors in the capsules.

We investigated the nitrogen behaviour in silicate melt using two different experimental setups.

We used the internally heated pressure vessel equipped with drop quench at the Earth Sciences Institute of Orleans (Iacono-Marziano et al., 2009). Within the furnace heated by molybdenum wires, the temperature is monitored by two Pt thermocouples. A platinum/rhenium quench wire was used as hanging wire. The temperature of most experiments was 1200°C, while for the experiment (AR5SiNFeN, AR5SiNFeNx2, PCR2SiNFeN), with nitrogen added as a mix of $Fe_{3.5}N$ and Si_3N_4, the temperature was 1300°C in order to avoid nucleation of olivine and clinopyroxene (Table 1). These experiments were conducted under gas pressure. The gas was composed of a mixture of

argon and hydrogen. Between the different runs, we changed the hydrogen fraction of the mixed gas in order to control the oxygen fugacity following this reaction (Gaillard et al., 2003):

$$H_2 + \frac{1}{2}O_2 = H_2O \tag{5}$$

One experiment was carried out in a half-inch piston cylinder assembly at a pressure of 10 kbar (1 GPa) and a temperature of 1300°C (Table 1). The starting basalt was placed into a AuPd capsule and doped in nitrogen with a mix of $Fe_{3,5}N$ and Si_3N_4 powders. The capsule was contained in an alumina sleeve and was sandwiched between a top and a bottom alumina plug. Temperature was monitored by two PtRh (platinum-rhodium) thermocouples. The alumina sleeve was placed in an assemblage composed of a succession of graphite pyrex and talc cylinders.

2.3. Analytical techniques

2.3.1. Electron microprobe analysis (EPMA)

EPMA analyses aimed at obtaining the chemical composition of silicate glass, minerals (olivines, clinopyroxenes) and metal alloys. Two different programs were used, one for analysis of the silicate glasses and the second one for the analysis of the iron alloys. The list of analysed elements of the two programs are listed in the Table 2. The setting for analysis was 15 kV and a current of 10 nA. Focused and defocused beams (5,10,20 μm)

were used depending on the analysed phase (resp. alloy and glass). The counting time for each component varied with their concentrations, more the element was concentrated in the silicate glass least the counting time was (few seconds).

2.3.2. Infrared analysis

The H_2O and CO_2 concentrations were determined by transmission Fourier Transform Infrared Spectroscopy (Iacono-Marziano et al., 2012; Shishkina et al., 2010) on doubly polished samples with the thicknesses varying between 80 to 130 µm. The micro-FTIR measurements were performed using a Nicolet Continuum microscope coupled to a Nicolet 6700 FTIR spectrometer. The device is equipped with Globar light source, XT-KBr beamsplitter, liquid N_2 cooled MCT-A detector, 32x infinity corrected Schwarzschild objective matching to 32x condenser. The spectra were recorded between 6000-1200 cm^{-1} with CaF_2 support and 4000-650 cm^{-1} with NaCl support in order to detect H_2O (3500, 4500 and 5200 cm^{-1}) and CO_2 (1515-1430 cm^{-1}) absorption bands, respectively.

2.3.3. fO_2 determination

Oxygen fugacity (fO_2) is an important parameter controlling the nitrogen behaviour in silicate melts (Boulliung et al., 2020; Dalou et al., 2019b; Grewal et al., 2020; Libourel et al., 2003; Speelmanns et al., 2019). Here, we use three techniques to determine the experimental fO_2 conditions. The sensor technique (Taylor et al., 1992), measuring the fO_2 at water saturation, uses two pellets of a Nickel Palladium or Cobalt Palladium alloy with zircon

powder and 10-20 mg of distilled water (Gaillard et al., 2003). We call this parameter "external fO$_2$" because it is measured in separate platinum capsule. This external fO$_2$ does not correspond to the fO$_2$ seen by each sample in their own capsule but it represents the fO$_2$ of a virtual sample in which water activity would be 1.

In order to account for the fact that water activity in our samples was less than 1, the fO$_2$ was calculated with the equilibrium (5). The law mass action for this equilibrium allows the fO$_2$ prevailing in each experimental charge to be related to the experimental fH$_2$O and fH$_2$.

$$K_5 = \frac{f_{H_2O}^{melt}}{f_{H_2}^{melt} \cdot fO_2^{\frac{1}{2}}} \tag{6}$$

$$logfO_2 = 2 \times (logf''_{2O} - logK_5 - logfH_2) \tag{7}$$

Water fugacity (fH$_2$O) is calculated using the model of (Iacono-Marziano et al., 2012) and the water content in silicate glasses (Table 3). We estimated the precision on fO$_2$ using this method as:

$$\Delta logfO_2 = \frac{2}{\ln(10)} * \frac{fH_2}{fH_2O} * \sqrt{\frac{\Delta fH_2O^2}{fH_2^2} + \frac{fH_2O^2 * \Delta fH_2^2}{fH_2^4}} \tag{8}$$

In order to directly probe the "internal fO$_2$" specific to each sample, we used metal-silicate equilibria implying the fO$_2$.

$$Fe + \frac{1}{2}O_2 = FeO \tag{9}$$

Oxygen fugacity can be calculated from the equilibrium (9) involving the activity of FeO in the silicate melt, the activity of Fe in the alloy and the equilibrium constant K_9 (Gaillard et al., 2003).

$$K_9 = \frac{a_{FeO}^{melt}}{a_{Fe}^{alloy} \cdot fO_2^{1/2}} \tag{10}$$

From the equilibrium constant and with $a_{FeO}^{melt} = \gamma_{FeO}^{melt} \cdot X_{FeO}^{melt}$ and $a_{Fe}^{alloy} = \gamma_{Fe}^{alloy} \cdot X_{Fe}^{alloy}$ the fO_2 is calculated with the equation (Medard et al., 2008).

$$\log fO_2 = \frac{2}{\ln(10)} (\ln\left(\frac{X_{FeO}^{melt}}{X_{Fe}^{alloy}}\right) - \ln(\gamma_{Fe}^{alloy}) + \ln(\gamma_{FeO}^{melt}) - \ln K_9) \tag{11}$$

The alloys in our experiment were mainly iron palladium (Fe-Pd) and iron iridium (Fe-Ir), with iron concentrations higher than 90% for the most reduce samples (AR5SiNFeN, AR5SiNFeNx2, PCR2SiNFeN see Table 2). The activity coefficient (γ) of iron for the Fe-Ir alloy was determined using equation from Woodland and O'Neill, 1997, for the Fe-Pd alloy, the activity coefficient of Fe was taken from (Aukrust and Muan, 1962). The equation used for the propagation of uncertainties for the internal fO_2 calculations is:

$$\Delta \log fO_2 = \frac{2}{\ln(10)} * \frac{aFe}{aFeO} * \sqrt{\frac{\Delta aFeO^2}{aFe^2} + \frac{aFeO^2 * \Delta aFe^2}{aFe^4}} \tag{12}$$

2.3.4. Volatiles in the glasses and composition of the fluid phase

Knowledge of the nitrogen pressure $P(N_2)$ or fugacity fN_2 in the fluid phase during the experiment is fundamental. Conversely to the low-pressure experiments (1 bar; (Boulliung et al., 2020; Libourel et al., 2003; Miyazaki et al., 2004), the nitrogen pressure in our experiment cannot be considered during the experiment as the fraction of N_2 injected in the gas mixture.

Hence, we calculated the fluid phase $P(N_2)$ in our high pressure experiments by quantifying the partial pressure of the other species composing the fluid phase. In our low pressure experiments (T>1200°C, P<2.5 kb), we assume the ideal mixing of ideal gaseous species of N_2, H_2O, CO_2, CO, H_2 (see also Iacono-Marziano et al., 2012).

The pressure of H_2O and CO_2 was determined after FTIR analysis (Table 4). The intensity of the IR band was converted in concentration of these elements in the silicate glass following (Shishkina et al., 2010). The calculated concentration was then converted into partial pressure of H_2O and CO_2 using the numerical model taken from (Iacono-Marziano et al., 2012). The P(CO) was determined using the activity of C (graphite) and the fO_2 of the experiment using the equilibrium: $C + \frac{1}{2} O2 - CO$. The $P(N_2)$ was then calculated by subtracting the fugacity of the other species cited before to the "total pressure" of the experiment. The $P(N_2)$ was then converted into nitrogen fugacity, fN_2, applying a 1.5 fugacity coefficient for N2 at 2.4 kbar (calculated according to Belonoshko and Saxena, 1992). For the high pressure piston cylinder experiment however, the N_2-fugacity coefficient was significant $\gamma_{N2} \approx 5,6$ (calculated according to Belonoshko and Saxena, 1992) for N_2.

2.3.5. Secondary ion mass spectrometry (SIMS)

The nitrogen (^{14}N) concentration of the quenched glasses was measured by secondary ion mass spectrometry (SIMS) at the CRPG (Nancy, France), using the CAMECA 1280 HR2 ion microprobe (Füri et al., 2018). Polished glass fragments were mounted in indium and coated with a thin layer of carbon. The sample mount was stored for 48h under vacuum in the airlock of the SIMS to remove any terrestrial adsorbed water before analysis.

Spot analyses of $^{14}N^{16}O^-$ secondary ions were carried out at a nominal mass resolution m/Δm

= 13'000 with a 10 kV Cs^+ primary ion beam, a current of ~10 nA, and a normal-incidence

electron gun to compensate the charge at the surface of the sample. Basaltic, Fe-free

glasses with N contents between <1 and 3906 $\pm$ 188 ppm N (as determined by static mass

spectrometry analysis at the CRPG noble gas facility; Humbert, 1998) were used as

reference materials to calibrate the secondary ion intensity ratio $^{14}N^{16}O^-/^{16}O_2^-$ to the nitrogen

abundances of the glasses. This method has been confirmed to yield nitrogen concentrations

in silicate glasses of variable composition (synthesized at fO_2 = IW-8 to IW+4.1, T = 1425°C,

P = 1 bar) that are in excellent agreement with static mass spectrometry measurements

(Boulliung et al., 2020), for a wide range of N contents between ≤1 to ~6000 ppm; therefore,

any matrix effects on the yields of secondary molecular ions ($^{14}N^{16}O^-$ and $^{16}O_2^-$) are

considered to be negligible. To verify the homogeneity of the N distribution, three spot

analyses were performed for each glass sample.

3. Results

3.1. Description of the run products

Most experimental products were crystal-free silicate glasses (Table 2). Only samples

AR1FeN and AR1HNO3C showed a very small amount of olivine and pyroxene crystals.

These crystals were observed in run number 1, synthesised at 1200°C, while at 1300°C the

experimental charge was crystal-free. The presence of bubbles was noticed in all samples

(Table 3, Fig. 1). These bubbles prove the attainment of fluid saturation during the experiment.

Another important point was the presence of droplets of metal alloy in some samples (Fig. 1), i.e., the most reduced ones and the one with added palladium powders (Table 3). These alloys were important for the fO_2 calculation of the samples. In agreement with previous work (Kadik et al., 2011; Speelmanns et al., 2019), we also observed metal micro-nuggets in the most reduced samples (AR5SiNFeNx2; fO_2<IW-3.5). They were, however, too small to be analysed.

(1
)

3.2. Composition of the experimental products and fluid phase

The glass compositions of our run products are reported in Table 2. Most of them were synthetized using internally heated pressure vessel experiments ('AR') and one using the piston cylinder experiment ('PCR'). In most cases, the chemical compositions of the silicate glasses were similar to the AR3HNO3C composition. Major compositional differences were however for the samples with Si_3N_4: those samples were enriched in SiO_2 with increase from 48 wt% to more than 54 wt%. For these extremely reduced samples, the FeO concentration is low (≈1 wt%) and we noticed many iron alloy nuggets (Table 3, e.g., samples AR4, AR5, PCR2). The volatile concentrations and oxygen fugacity of the different samples are reported in Table 3. In general, the samples were too CO_2-poor to permit detection. Significant amounts of CO_2 were only measured in samples AR3HNO$_3$C, AR4NH$_3$FeSCIr, and AR4HNO$_3$CPd that were graphite saturated, and in which nitrogen was added in the form of an aqueous solution (Table 3). The water concentration is strongly correlated with the fO_2 as

expected from equilibrium (5). The highest H_2O concentrations were measured in the samples doped in nitrogen as an aqueous solution (e.g., AR1NH₃, AR3HNO₃C, AR3HNO₃AgCO, AR4NH₃FeSCIr, AR4HNO₃CPd). In addition to the volatile concentration of the samples, we also determined the composition of the fluid for each of them. Table 4 reports the fugacity of each component in the fluid in equilibrium with the silicate melt during the experiments. Samples with nitrogen added as an aqueous solution present the highest water and CO_2 fugacities. For these samples, the fluid phase was a multicomponent mixture, while the samples AR5SiNFeN and AR5SiNFeNx2 with addition of nitrogen as silicon nitride powders were mostly anhydrous and their fluid phase was essentially composed of nitrogen (N_2). The PC experiment has a fluid phase composed mainly of nitrogen species. The CO_2 concentration below the detection limit of the IR analysis (a few ppm) and the H_2O concentration at 500 ppm indicates that in the fluid phase the fugacity of these elements is very low (<1 bar and $fH_2 \approx 3$ bar) compared to the total pressure (10000 bar). We therefore consider that $P(tot) = P(N_2)$ and the fugacity coefficient (see above) at P and T was used to calculate fN_2. The uncertainty on the nitrogen pressure measurement hence corresponds to the uncertainty on the pressure measurement of the machine ($\pm10\%$).

3.3. fO_2 (ΔIW) results

For the samples with fO_2 calculated using the two methods (i.e., Eqns. 7 and. 11), we compared the result to check the internal consistency and to validate the attainment of equilibrium (Table 5). In most cases, the difference between the log fO_2 values was very small and within the quoted uncertainties, i.e., between 0.1 and 0.4 log units.

The biggest variation between the two internal fO_2 values was observed for the sample synthesized during run 5, which is characterized by the lowest water content (0.02 and 0.04 wt%, Table 3). For these samples, the treatment of IR spectra was difficult due to the very low intensity of the peak (0.041±0.017 Abs AR5SiNFeN, 0.054±0.011 Abs PCR2SiNFeN). Nevertheless, for each sample, the differences between calculated fO_2 are within or close to the propagated uncertainties.

Experiments doped in nitrogen with a mix of Si_3N_4 and $Fe_{3.5}N$ seems to be the best way to produce fO_2 conditions below the IW buffer (Dalou et al., 2017). For the other experiments doped with other nitrogen sources such as aqueous solution, the fO_2 are more oxidised (+1.97<log fO_2 (ΔIW) <+4.91), consistent with the presence of large amounts of water. When fO_2 constraints from both methods of calculations were available, we used the internal fO_2 value from Fe/FeO equilibrium in the following discussion (i.e., eq. 11).

3.4. Nitrogen concentration

Nitrogen concentrations at fluid saturation (Table 3) are shown in Figure 2 together with the results of previous studies supposed to be fluid saturated at low pressure (Boulliung et al., 2020; Libourel et al., 2003; Miyazaki et al., 2004), medium pressure (Li et al., 2015) and high pressure (Grewal et al., 2019; Speelmanns et al., 2019). Nitrogen concentrations in our samples vary between 5 and >1000 ppm. The low N-concentration samples (3.6 ± 1.9 to 26.3 ± 5.3 ppm) were obtained for the most oxidizing condition (fO_2>IW). In this fO_2 domain, N content weakly varies with fO_2, because nitrogen is mainly dissolved physically as N_2. For the reduced samples (fO_2<IW-2), the N content in the glasses increases with decreasing fO_2

and attains, for the most reduced sample (AR5SiNFeNx2), 1737 ± 112 ppm at IW-4.5. These observations indicate that nitrogen concentrations are correlated with variation in fO_2 only for conditions below IW-1.5: under these conditions, if the fO_2 continue to decrease, the nitrogen concentration increases drastically.

4. Discussion

4.1. Attainment of equilibrium

To demonstrate that the equilibrium of our experiments was reached, the homogeneity of our samples was verified using different methods. Firstly, we check the homogeneity of the major elements through the chemical composition of our silicate glass (SiO_2, Al_2O_3,…), if the glass shows good homogeneity, this indicates that the latter was in equilibrium. The second important point to verify is the homogeneity of the nitrogen concentration within the sample in order to see if the nitrogen had sufficient time to diffuse in the sample in a homogeneous way. The third point is the convergence of the internal fO_2 value read with the two techniques explained in section 3.3. Only if these three elements are verified we validate the achievement of equilibrium during the experiment. In addition, a comparison with the equilibrium data taken in the literature is carried out to check consistency.

For our study, by referring to the different tables (Table 2, 3, 5) we can verify this attainment of equilibrium for all samples. The chemical composition (SiO_2, FeO, …) of the different sample shows a good spatial homogeneity, with minor compositional variation between the different analysis points (Cf. Table 2.). This observation can also be made for the

concentrations of volatile elements including nitrogen, the concentration only weakly varies between the different analysis points (Cf. Table 3.). Regarding to the internal fO_2 values obtain by the two different calculation ways, i.e. water activity and Fe/FeO activities, the equilibrium seems to be reach due to the similar results of these two techniques (Cf. Table 5.). Lastly when we compare our point with those of previous studies, we notice that our points are part of a logical trend of those already obtained by previous studies. Our nitrogen concentration evolves in a way similar to that of Libourel et al. (2003), with higher concentrations, linked to pressure and therefore nitrogen fugacity differences (i.e. 1 atm vs 800 bar). Our high-pressure anchor point (Cf. Figure 2. blue circle) is also within the nitrogen concentration ranges observed by other high-pressure studies (i.e. Grewal et al., 2019; Speelmanns et al., 2019).

4.2. Nitrogen species and solubility as a function of fO_2 and pressure

Figure 2 shows that pressure has a major effect on the nitrogen solubility for all investigated conditions of oxygen fugacities. For $fO_2>\Delta IW$, no fO_2-dependency is observed with similar trends observed at low pressure (1 bar; Libourel et al., 2003) and in our experiments performed at medium pressures (i.e., 0.8 and 2.4 kbar). However, our data are shifted by two to three log-units upward in term of nitrogen concentration. At $fO_2>IW$, our results show similar N-concentrations than those reported in previous study (Li et al., 2015, ~10 ppm), thus confirming the lack of fO_2 dependence. There is therefore a significant effect of pressure and independently of the nitrogen fugacity; with a general increase of one log unit in N-content as pressure increases by one order of magnitude. A similar trend can be

observed in experiments performed at higher pressures (Grewal et al., 2019; Speelmanns et al., 2019), with a comparable increase of N concentration at higher pressures (Fig. 2). Fig. 2 also shows the duality of N-solubility behaviour, reflecting most likely (i) a physical, fO_2-independent, N_2 dissolution under oxidising conditions (> IW-1.5) and (ii) a chemical dissolution of N^{3-} that is strongly enhanced at the most reduced conditions. The hypothesis of a dual N-speciation, described first by (Libourel et al., 2003) at atmospheric pressure, seems to be confirmed at medium pressure within our experimental data.

4.3. Calibration of the solubility model

We have compiled a database containing nitrogen concentrations in melts of different experimental studies at different pressures temperatures and fO_2 conditions. We only use the data of nitrogen concentration in basaltic melts that we assume to be equilibrated at fluid saturation (an assumption that could be verified for studies containing the relevant information). In addition to our experiments, the database contains data from low pressure (Libourel et al., 2003; Miyazaki et al., 2004), medium pressure (Li et al., 2015) and high pressure experiments (≥1.5 GPa; Grewal et al., 2019; Speelmanns et al., 2019). The parameters of the database were: nitrogen contents in the melt, temperature (°C, K), pressure (bar), oxygen fugacity (fO_2, log fO_2, log fO_2 (ΔIW) and the nitrogen fugacity (fN_2). We restricted the database to studies with similar starting material (≈basalt), in order to reduce the potential effect of the NBO/T on the nitrogen solubility (Mysen et al., 2008; Roskosz et al., 2006; Boulliung et al., 2020). We have also dismissed some studies that investigated nitrogen metal-silicate partitioning because they have no proof of fluid in the

synthesized samples (such as bubbles trapped in the glass e.g Dalou et al., 2019b, 2017).

Using this database, we can represent the effect of nitrogen pressure on nitrogen solubility

(Fig. 3). The nitrogen concentration data used for figure 3 are for conditions more oxidizing

than IW-2 in order to restrict the effect of fO_2. In agreement with previous observations

(Roskosz et al., 2006), the nitrogen concentration appears to increase as the pressure, and

therefore the nitrogen fugacity increases. This observation is valid for reduced and oxidized

conditions and suggests that N_2 remains the dominant N-species in the fluid for all these

experimental studies. According to Chen et al. (2019), the N_2 species fraction in the fluid

increases with fO_2. In addition, an increase of the temperature and/or the total nitrogen

concentration in the fluid phase appears to increase the N_2 fraction in the fluid at the expense

of NH_3. In contrast, a pressure rise will increase the NH_3 fraction in the fluid (Chen et al.,

2019). When we extrapolate the result of Chen et al. (2019) to the conditions of the

experimental data in Figure 3, the main species present in the fluid tends to be N_2.

The two dissolution reactions used for the N-solubility model are:

$$N_{2(gas)} = N_{2(silicate\ melt)} \tag{13}$$

$$\frac{1}{2}N_{2(gas)} + \frac{3}{2}O^{2-}_{(silicate\ melt)} = N^{3-}_{(silicate\ melt)} + \frac{3}{4}O_{2(gas)} \tag{14}$$
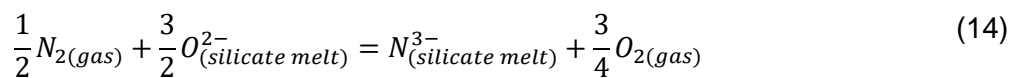
Reaction 13 corresponds to the physical dissolution of N_2, whereas reaction 14 corresponds

to the chemical dissolution of N^{3-}. The total nitrogen concentration in the silicate melt

corresponds to the sum of the two species concentration.

$$[N_{calc}] = [N_2] + [N^{3-}] \tag{15}$$

From the eq. 13, we can calculate the N_2 concentration, which mainly depends on nitrogen fugacity:

$$[N_2] = K_{13} * fN_2 \tag{16}$$

From the eq. 14, we can calculate the N^{3-} concentration, which mainly depends on fO_2 and fN_2:

$$[N^{3-}] = fO_2^{-3/4} * K_{14} * fN_2^{1/2} \tag{17}$$

The eq. 16 and 17 once replaced in eq. 15 allows us to propose the nitrogen concentration in silicate melt as:

$$[N_{calc}] = K_{13} * fN_2 + fO_2^{-3/4} * K_{14} * fN_2^{1/2} \tag{18}$$

The thermodynamic constants (K_{13}, K_{14}) of the two reactions follow this form

$$K = \exp(\frac{-\Delta r G^{P,T}}{RT}) \tag{19}$$

where

$$\Delta r G^{P,T} = \Delta r H - T \Delta r S + P \Delta r V \tag{20}$$

P and T correspond to the pressure (bar) and temperature (K) of the system. In the eq. 20, $\Delta r G^{P,T}$ corresponds to the Gibbs free energy of the reaction for given and variable P and T

values, calculated with, ∆rH the enthalpy, ∆rS the entropy and ∆rV the volume of the reaction at P and T. All the thermodynamic constants were adjusted using the low, medium and high-pressure data and the result is given in Table 6.

We assumed that the enthalpy and entropy are constant over the T range, although this assumption was not applied to the volume changes of reaction (13) and (14). The following correction was applied in the P-range 0-1 GPa:

$$\Delta V = \Delta V + P\,\Delta V' \tag{21}$$

At P> 1GPa, the volume changes are considered constant.

The constants ΔH_{13}, ΔS_{13} and ΔV_{13} were used for the calculation of the K_{13} and characterise the physical dissolution of N_2 in the silicate melt. ΔH_{14}, ΔS_{14} and ΔV_{14} were used for the calculation of K_{14} and therefore characterise the chemical dissolution of N^{3-}. These two sets of constants were calibrated using two different functions $F_{opti}13$ for ΔH_{13}, ΔS_{13}, ΔV_{13} and $F_{opti}14$ for ΔH_{14}, ΔS_{14}, ΔV_{14} of the form

$$F_{opti}13 = \sum \frac{|\,N_{mes} - N_{calc}\,|^2}{\sigma_{N_{mes}}} \tag{22}$$

$$F_{opti}14 = \sum \frac{|\,N_{mes} - N_{calc}\,|^2}{\sigma_{N_{mes}}} + \frac{|\,fO_{2\,mes} - fO_{2\,calc}\,|^2}{\sigma_{N_{mes}}} * 0.01 \tag{23}$$

$F_{opti}13$ was used to minimize the difference between the measured and the calculated N concentration for the most oxidised data (>IW-1.5). $F_{opti}14$ was used to minimize the difference in term of nitrogen concentration and oxygen fugacity for the most reduce data

(<IW-1.5). This formalism allowed us to produce a model taking into account both uncertainties in N content and fO_2.

The error estimation for the 6 constants presented in the Table 6 is calculated for an increase in the residue on the fitting function presented above of 30%. This threshold allows us to determine the range of variation (maximum and minimum values) for each of our constants. This 30% threshold is comparable to the average value of the uncertainty in the measurement of nitrogen contents in glasses (31%) in the compiled database.

Results obtained experimentally and calculated by the model were then compared in two different ways. First, we compare the calculated data to the analysed nitrogen concentration in the silicate melt as a function of fO_2 (ΔIW; Fig. 4).

The results of the model are in good agreement with experimental data (Fig. 4). If we compare the calculated nitrogen concentration to the measured data (Fig. 4), we obtain a data array aligned along a straight line of slope 1 (R2 = 0.96). These observations support the accuracy of the calculated data.

In details, we see that the solubility model captures well the trend. However, for some data points, the differences between the calculated and measured data exceed the uncertainties which is likely due to some uncertainties in the composition of the fluid phase of the experiments used for the calibration.

The 2-species model first presented by Libourel et al. (2003) at a pressure of 1 bar is validated here to moderately high pressure in a C-H-O-N system. The temperature range covered by the database is from 1100 to 2000°C, the pressure from 1 bar to 10000 bar and the fO_2 from IW-8 to IW+8. The chemical composition is mainly basaltic. The volume

changes of the two dissolution mechanisms are respectively positive and negative, which is consistent with fact that the volume change of reaction (13) is the partial molar volume of N_2 (being positive), while the volume change of reaction (14) is the difference between the volume of N^{3-} and 3/2 the volume of O^{2-} (being negative). In detail, we notice that the fitted partial molar volume of N_2 in the silicate melt is close to the partial molar volume of N_2 liquid at 1 atm. and its boiling point (i.e., 34.5 cc/mol. = 3.5 J/bar). Although the fluid phase of the model was assumed to be N_2-dominated (it does not take into account the presence of NH_3 in the fluid phase), our model also adequately describes the N-solubility at low pressure to moderately high-pressure. A more complicated model including NH_3 in the fluid is not required at this stage, probably due to the fact that most experiments performed under reduced conditions are generally dry (Table 5), implying low fH_2 conditions. Since the NH_3/N_2 speciation is ruled by the respective equilibria:

$$N_2 + 3H_2O = 2NH_3 + 3/2O_2 \tag{23}$$

or

$$N_2 + 3H_2 = 2NH_3 \tag{24}$$

it clearly appears that low fH_2 (and low fH_2O) strongly reduces the presence of NH_3. NH_3 is also precluded by the high N-content of our fluid phase, the high temperature and the moderately high-pressure condition, in agreement with previous observations (Chen et al., 2019).

A second working hypothesis concerns the nitrogen species in the silicate melt. We considered two main species: N_2 and N^{3-}. Several previous studies (Dalou et al., 2019b;

Grewal et al., 2020; Kadik et al., 2015; Mosenfelder et al., 2019) suggested the presence of

NH_x species where N has the valence of N^{3-}. Here, a two-species model (N_2 and N^{3-})

adequately describes the fO_2-P-T dependence of N-solubility. No attempt to parameterize an

NBO/T parameter was considered though a significant effect of NBO/T on N-solubility was

previously underlined (Mysen and Fogel, 2010; Boulliung et al., 2020). Here, this parameter

has not been considered because in agreement with the observations of the articles

Boulliung et al. (2020), for the fO_2 conditions of most of the points used by the database (i.e.

>IW -5,1), the NBO / T has an impact that is still difficult to define and requires more work.

For the time being, this model is accurate for describing the available database. However,

this model will have to consider other melt and fluid species once their P-T-fO_2 domain will be

better defined. In particular, data at low N content or at least at low N/H and low N/C are

needed.

4.4. Model application to melt degassing processes

Eq. 18 permits the prediction of nitrogen solubility in a basaltic melt in the P-fO_2 parameter

space. For a constant temperature of 1200°C, we can make a series of isobars of nitrogen

fugacity on a diagram nitrogen concentration as a function of fO_2 (Fig. 6). Fig. 6 shows that

both N_2 and N^{3-} species have solubilities that increase with increasing nitrogen pressure. In

details, the fO_2 at which speciation changes from N_2 to N^{3-} decreases as pressure increases.

At low pressure, the N_2-N^{3-} transition occurs at IW, while at 3 GPa, it occurs at IW-3. There is

therefore a shift of 1-log unit in fO_2 per GPa of the boundary separating the N_2 dominated

from the N^{3-} dominated area. This shift can be explained by the dependence on $P(N_2)$ of the solubility of both N_2 and N^{3-} species (Eqns. 16 & 17). N_2 dissolution mechanism has a +1 exponent on $P(N_2)$ while N^{3-} dissolution mechanism has a 0.5 exponent dependence on $P(N_2)$. This implies that the fO_2 domain where the N-speciation shifts from N_2 to N^{3-} must change with $P(N_2)$ rather than total pressure.

Degassing of Earth's magma ocean is supposed to have occurred at fO_2 conditions ranging from IW-5, at the beginning of the magma ocean stage, to IW-2 for the lastest stages (Wood et al., 2006). This is deduced from metal partitioning during core – mantle equilibration processes, but admittedly, after the core segregation, the magma ocean could have evolved more oxidized. At IW-5 and fluid saturation, the nitrogen content in the silicate melt is ca. 3000 ppm (0.3 wt%) for fN_2 of 100 bar (see Fig. 6). At IW-2, corresponding to the last stage of magma ocean-core equilibration, the nitrogen content in the silicate melt for a similar fN_2 decreases and attains 10 ppm (0.001 wt%). This implies a drastic change of the nitrogen behaviour during this period of core mantle segregation. According to Speelmanns et al. (2018), nitrogen became increasingly siderophile during the last stage of the core-magma ocean segregation (i.e., as the oxygen fugacity evolved from ΔIW-5 to IW-2). However, as the magma ocean went through this redox interval (from ΔIW-5 to ΔIW -2), nitrogen became also more atmophile as shown by Figure 6. This is because the oxidation state of N in metal and the gas phases is similar (zero). These two phenomena, N incorporation in metal vs. N degassing, thus entered in competition at the end of the core mantle equilibration at ca. IW-2. This made more difficult the incorporation of N in the core. In summary, at very low fO_2, N is neither siderophile nor atmophile, it is magmatophile, while at intermediate fO_2 (IW-2), N is

siderophile and atmophile. We note that planetary systems experiencing very low fO_2 (ie. IW-5) during their magma ocean and post-magma ocean stages, such as Mercury, may accordingly contains high nitrogen content in their mantle. In contrast, planets like Earth and Mars, that experienced core-magma ocean equilibration close to IW-2, must have little N contents in their mantle.

4.5. Nitrogen impact on the volcanism of planets with reduced magmatic conditions

As explained above, under reduced conditions nitrogen is magmatophile (not siderophile, nor atmophile), implying that reduced magma oceans must crystallize under high N-activity while oxidized magma oceans would solidify under low N-activity. No melt-crystal N-partitioning experiments exist. However, some studies, which focus on the nitrogen solubility in mantle minerals (Li et al., 2013; Yoshioka et al., 2018), compare their solubility results for mantle minerals with data of nitrogen solubility in silicate melt of previous studies (Libourel et al., 2003; Miyazaki et al., 2004; Roskosz et al., 2013). From these comparisons, the two minerals studies deduce mineral-melt nitrogen partitioning, one of the important criteria for discussing nitrogen degassing.

Since nitrogen can be incorporated into mantle minerals (Li et al., 2013; Yoshioka et al., 2018), we may assume that a solidifying magma ocean can sequester nitrogen in its mantle. In turn, assuming that N is incompatible upon partial melting (which is likely at fO_2 <IW-3), it can be incorporated into the liquid and transported to the surface. High N-content

in the melt may impact the degassing process during the magma ascent and, *in fine*, the eruption. However, such features are not relevant for the current volcanism on Earth or Mars due to oxidising condition (≈IW to FMQ; Righter et al., 2008) yielding low nitrogen concentrations in their cooling magma oceans. For a planet with strongly reduced conditions like Mercury, where the fO_2 of its interior was estimated to be between ΔIW-6.3 to -2.6 (McCubbin et al., 2012) or ΔIW-7.3 to -4.5 (Zolotov et al., 2013), nitrogen can be highly concentrated in the silicate melt with contents exceeding 1000 ppm. In addition, the low fO_2 conditions of Mercury do not allow the stability of species such as H_2O or CO_2 but favour the stability of volatile species such as S_2, CO and CH_x by increasing the H_2/H_2O and C/O ratio (Cartier and Wood, 2019; Ebel and Alexander, 2011; Zolotov, 2011). According to our data and previous formalism for reduced conditions (i.e., IW<-6, Zolotov, 2011) several wt% of N are lost by a pressure drop of 1kbar (red arrow fig. 6). It is therefore likely that, under these conditions, nitrogen was one of the main volatile species, which can impact the eruptive dynamics on Mercury similarly to water for Earth.

5. Conclusion

This new experimental study provides constraints on the solubility of nitrogen in basaltic melts at fluid-saturation under lithospheric pressure. It indicates that for the most oxidised conditions, nitrogen solubility is low and depends mainly on the nitrogen pressure (N_2 dissolution). For the most reduced conditions (<IW), nitrogen solubility increases drastically and is correlated to the decrease in fO_2 (N^{3-} dissolution). These observations corroborate a previous studies at low pressure (Libourel et al., 2003; Boulliung et al., 2020). A two species solubility model (N_2, N^{3-}) of nitrogen in silicate melt was calibrated with our data and previous data for fluid saturated conditions (Grewal et al., 2019; Li et al., 2015; Libourel et al., 2003; Miyazaki et al., 2004; Speelmanns et al., 2019). This model successfully reproduces most of the literature data at fluid saturation. However, we assumed some starting hypothesis (4.2.) that need to be verified against a larger set of experimental work. These results (experimental and modelled) emphasize that nitrogen degassing from a magma ocean must predominantly occur in the fO_2 range IW-9 to IW. Pressure is also an important parameter. A decrease of the nitrogen pressure leads to a decrease of the nitrogen solubility in the silicate melt (see eq. 17), thus contributing to degassing. On reduced planets like Mercury, nitrogen can be a trigger for explosive eruptions.

The solubility model must evolve in the future with new data at low nitrogen activity in order to test the presence of NH_3 in both melt and fluid phases. More data at high pressure and fluid saturation are also needed.

Nitrogen partitioning between the metal and the silicate melt is an additional important process to take into account. In most of the recent studies of the partitioning of nitrogen between silicate melt and liquid iron-alloy, nitrogen appears to be more siderophile when the condition become more oxidised (Dalou et al., 2019b; Speelmanns et al., 2019, 2018) and more lithophile at reduced conditions. We note a similar behaviour between silicate melt and fluid phase: when the condition becomes more oxidised, nitrogen becomes more atmophile. Future efforts must consider this complex three-phase issue: chemical exchange of N between the metal, the silicate melt and the gas phases.

Acknowledgements

References

Aukrust, E., Muan, A., 1962. Thermodynamic properties of Pd-Fe alloys in the Temperature range 1200-1460°C. Acta Metall. 10, 555–560.

Belonoshko, A.B., Saxena, S.K., 1992. A unified equation of state for fluids of C-H-O-N-S-Ar composition and their mixtures up to very high temperatures and pressures. Geochim. Cosmochim. Acta 56, 3611–3626. https://doi.org/10.1016/0016-7037(92)90157-E

Boulliung, J., Furï, E., Dalou, C., Tissandier, L., Zimmermann, L., Marrocchi, Y., 2020. Oxygen fugacity and melt composition controls on nitrogen solubility in silicate melts. Geochim. Cosmochim. Acta.

Cartier, C., Wood, B.J., 2019. The Role of Reducing Conditions in Building Mercury. Elements 15, 39–45. https://doi.org/10.2138/gselements.15.1.39

Catling, D.C., Zahnle, K.J., 2020. The Archean atmosphere. Sci. Adv. 6, eaax1420. https://doi.org/10.1126/sciadv.aax1420

Chen, Q., Zhang, Z., Wang, Z., Li, W.-C., Gao, X.-Y., Ni, H., 2019. In situ Raman spectroscopic study of nitrogen speciation in aqueous fluids under pressure. Chem. Geol. 506, 51–57. https://doi.org/10.1016/j.chemgeo.2018.12.016

Dalou, C., Füri, E., Deligny, C., Piani, L., Caumon, M.-C., Laumonier, M., Boulliung, J., Edén, M., 2019a. Redox control on nitrogen isotope fractionation during planetary core formation. Proc. Natl. Acad. Sci. 116, 14485–14494. https://doi.org/10.1073/pnas.1820719116

Dalou, C., Hirschmann, M.M., Jacobsen, S.D., Le Losq, C., 2019b. Raman spectroscopy study of C-O-H-N speciation in reduced basaltic glasses: Implications for reduced planetary mantles. Geochim. Cosmochim. Acta 265, 32–47. https://doi.org/10.1016/j.gca.2019.08.029

Dalou, C., Hirschmann, M.M., von der Handt, A., Mosenfelder, J., Armstrong, L.S., 2017. Nitrogen and carbon fractionation during core–mantle differentiation at shallow depth. Earth Planet. Sci. Lett. 458, 141–151. https://doi.org/10.1016/j.epsl.2016.10.026

Ebel, D.S., Alexander, C.M.O., 2011. Equilibrium condensation from chondritic porous IDP enriched vapor: Implications for Mercury and enstatite chondrite origins. Planet. Space Sci. 59, 1888–1894. https://doi.org/10.1016/j.pss.2011.07.017

Füri, E., Deloule, E., Dalou, C., 2018. Nitrogen abundance and isotope analysis of silicate glasses by secondary ionization mass spectrometry. Chem. Geol. 493, 327–337. https://doi.org/10.1016/j.chemgeo.2018.06.008

Gaillard, F., Schmidt, B., Mackwell, S., McCammon, C., 2003. Rate of hydrogen–iron redox exchange in silicate melts and glasses. Geochim. Cosmochim. Acta 67, 2427–2441. https://doi.org/10.1016/S0016-7037(02)01407-2

Gennaro, E., Iacono-Marziano, G., Paonita, A., Rotolo, S.G., Martel, C., Rizzo, A.L., Pichavant, M., Liotta, M., 2019. Melt inclusions track melt evolution and degassing of Etnean magmas in the last 15 ka. Lithos 324–325, 716–732. https://doi.org/10.1016/j.lithos.2018.11.023

Grewal, D.S., Dasgupta, R., Farnell, A., 2020. The speciation of carbon, nitrogen, and water in magma oceans and its effect on volatile partitioning between major reservoirs of the Solar System rocky bodies. Geochim. Cosmochim. Acta 280, 281–301. https://doi.org/10.1016/j.gca.2020.04.023

Grewal, D.S., Dasgupta, R., Holmes, A.K., Costin, G., Li, Y., Tsuno, K., 2019. The fate of nitrogen during core-mantle separation on Earth. Geochim. Cosmochim. Acta 251, 87–115. https://doi.org/10.1016/j.gca.2019.02.009

Humber F. (1998) Solubilité de l'azote dans les silicates liquides influence de la fugacité d'oxygène et de la composition, Ph. D. thesis. Henri Poincaré- Nancy 1 University.

Iacono-Marziano, G., Morizet, Y., Le Trong, E., Gaillard, F., 2012. New experimental data and semi-empirical parameterization of H2O–CO2 solubility in mafic melts. Geochim. Cosmochim. Acta 97, 1–23. https://doi.org/10.1016/j.gca.2012.08.035

Kadik, A.A., Koltashev, V.V., Kryukova, E.B., Plotnichenko, V.G., Tsekhonya, T.I., Kononkova, N.N., 2015. Solubility of nitrogen, carbon, and hydrogen in FeO–Na2O–Al2O3–SiO2 melt and liquid iron alloy: Influence of oxygen fugacity. Geochem. Int. 53, 849–868. https://doi.org/10.1134/S001670291510002X

Kadik, A.A., Kurovskaya, N.A., Ignat'ev, Yu.A., Kononkova, N.N., Koltashev, V.V., Plotnichenko, V.G., 2011. Influence of oxygen fugacity on the solubility of nitrogen, carbon, and hydrogen in FeO-Na2O-SiO2-Al2O3 melts in equilibrium with metallic iron at 1.5 GPa and 1400°C. Geochem. Int. 49, 429–438. https://doi.org/10.1134/S001670291105003X

Li, Y., Huang, R., Wiedenbeck, M., Keppler, H., 2015. Nitrogen distribution between aqueous fluids and silicate melts. Earth Planet. Sci. Lett. 411, 218–228. https://doi.org/10.1016/j.epsl.2014.11.050

Li, Y., Keppler, H., 2014. Nitrogen speciation in mantle and crustal fluids. Geochim. Cosmochim. Acta 129, 13–32. https://doi.org/10.1016/j.gca.2013.12.031

Li, Y., Wiedenbeck, M., Shcheka, S., Keppler, H., 2013. Nitrogen solubility in upper mantle minerals. Earth Planet. Sci. Lett. 377–378, 311–323. https://doi.org/10.1016/j.epsl.2013.07.013

Libourel, G., Marty, B., Humbert, F., 2003. Nitrogen solubility in basaltic melt. Part I. Effect of oxygen fugacity. Geochim. Cosmochim. Acta 67, 4123–4135. https://doi.org/10.1016/S0016-7037(03)00259-X

Marty, B., 2012. The origins and concentrations of water, carbon, nitrogen and noble gases on Earth. Earth Planet. Sci. Lett. 313–314, 56–66. https://doi.org/10.1016/j.epsl.2011.10.040

Marty, B., Zimmermann, L., Pujol, M., Burgess, R., Philippot, P., 2013. Nitrogen Isotopic Composition and Density of the Archean Atmosphere. Science 342, 101–104. https://doi.org/10.1126/science.1240971

McCubbin, F.M., Riner, M.A., Vander Kaaden, K.E., Burkemper, L.K., 2012. Is Mercury a volatile-rich planet?: VOLATILES ON MERCURY. Geophys. Res. Lett. 39, n/a-n/a. https://doi.org/10.1029/2012GL051711

Medard, E., McCammon, C.A., Barr, J.A., Grove, T.L., 2008. Oxygen fugacity, temperature reproducibility, and H2O contents of nominally anhydrous piston-cylinder experiments using graphite capsules. Am. Mineral. 93, 1838–1844. https://doi.org/10.2138/am.2008.2842

Miller, S.L., 1953. A Production of Amino Acids Under Possible Primitive Earth Conditions. Science 117, 528–529. https://doi.org/10.1126/science.117.3046.528

Miyazaki, A., Hiyagon, H., Sugiura, N., Hirose, K., Takahashi, E., 2004. Solubilities of nitrogen and noble gases in silicate melts under various oxygen fugacities: implications for the origin and degassing history of nitrogen and noble gases in the earth. Geochim. Cosmochim. Acta 68, 387–401. https://doi.org/10.1016/S0016-7037(03)00484-8

Mosenfelder, J.L., Von Der Handt, A., Furi, E., Dalou, C., Hervig, R.L., Rossman, G.R., Hirschmann, M.M., 2019. Nitrogen incorporation in silicates and metals: Results from SIMS, EPMA, FTIR, and laser-extraction mass spectrometry. Am. Mineral. 104, 31–46. https://doi.org/10.2138/am-2019-6533

Mysen, B.O., Fogel, M.L., 2010. Nitrogen and hydrogen isotope compositions and solubility in silicate melts in equilibrium with reduced (N+H)-bearing fluids at high pressure and temperature: Effects of melt structure. Am. Mineral. 95, 987–999. https://doi.org/10.2138/am.2010.3364

Mysen, B.O., Yamashita, S., Chertkova, N., 2008. Amorphous materials: Properties, structure, and durability: Solubility and solution mechanisms of NOH volatiles in silicate melts at high pressure and temperature--amine groups and hydrogen fugacity. Am. Mineral. 93, 1760–1770. https://doi.org/10.2138/am.2008.2879

Righter, K., Yang, H., Costin, G., Downs, R.T., 2008. Oxygen fugacity in the Martian mantle controlled by carbon: New constraints from the nakhlite MIL 03346. Meteorit. Planet. Sci. 43, 1709–1723. https://doi.org/10.1111/j.1945-5100.2008.tb00638.x

Roskosz, M., Bouhifd, M.A., Jephcoat, A.P., Marty, B., Mysen, B.O., 2013. Nitrogen solubility in molten metal and silicate at high pressure and temperature. Geochim. Cosmochim. Acta 121, 15–28. https://doi.org/10.1016/j.gca.2013.07.007

Roskosz, M., Mysen, B.O., Cody, G.D., 2006. Dual speciation of nitrogen in silicate melts at high pressure and temperature: An experimental study. Geochim. Cosmochim. Acta 70, 2902–2918. https://doi.org/10.1016/j.gca.2006.03.001

Shishkina, T.A., Botcharnikov, R.E., Holtz, F., Almeev, R.R., Portnyagin, M.V., 2010. Solubility of H2O- and CO2-bearing fluids in tholeiitic basalts at pressures up to 500MPa. Chem. Geol. 277, 115–125. https://doi.org/10.1016/j.chemgeo.2010.07.014

Speelmanns, I.M., Schmidt, M.W., Liebske, C., 2019. The almost lithophile character of nitrogen during core formation. Earth Planet. Sci. Lett. 510, 186–197. https://doi.org/10.1016/j.epsl.2019.01.004

Speelmanns, I.M., Schmidt, M.W., Liebske, C., 2018. Nitrogen Solubility in Core Materials. Geophys. Res. Lett. 45, 7434–7443. https://doi.org/10.1029/2018GL079130

Taylor, J.R., Wall, V.J., Pownceby, M.I., 1992. The calibration and application of accurate redox sensors. Am. Mineral. 77, 284–295.

Wood, B.J., Walter, M.J., Wade, J., 2006. Accretion of the Earth and segregation of its core. Nature 441, 825–833. https://doi.org/10.1038/nature04763

Woodland, A.B., O'Neill, H.St.C., 1997. Thermodynamic data for Fe-bearing phases obtained using noble metal alloys as redox sensors. Geochim. Cosmochim. Acta 61, 4359–4366.

Yoshioka, T., Wiedenbeck, M., Shcheka, S., Keppler, H., 2018. Nitrogen solubility in the deep mantle and the origin of Earth's primordial nitrogen budget. Earth Planet. Sci. Lett. 488, 134–143. https://doi.org/10.1016/j.epsl.2018.02.021

Zahnle, K., Schaefer, L., Fegley, B., 2010. Earth's Earliest Atmospheres. Cold Spring Harb. Perspect. Biol. 2, a004895–a004895. https://doi.org/10.1101/cshperspect.a004895

Zolotov, M.Yu., 2011. On the chemistry of mantle and magmatic volatiles on Mercury. Icarus 212, 24–41. https://doi.org/10.1016/j.icarus.2010.12.014

Zolotov, M.Yu., Sprague, A.L., Hauck, S.A., Nittler, L.R., Solomon, S.C., Weider, S.Z., 2013. The redox state, FeO content, and origin of sulfur-rich magmas on Mercury: SULFUR-RICH MAGMAS ON MERCURY. J. Geophys. Res. Planets 118, 138–146. https://doi.org/10.1029/2012JE004274

Table 1. Experimental conditions and starting mixtures of the runs presented in this study. 'A' stands for internally heated pressure vessel experiments and 'PC' for piston cylinder experiments. A Cobalt Palladium (CoPd) sensor was used for the experiments with the highest PH_2 pressure, whereas a Nickel Palladium (NiPd) sensor was used for low- PH_2 experiments.
(1) Description of the starting material B=Basalt, G=Graphite, Ir=Iridium, Pd=Paladium

Run	Sample ID	Starting material[1]	Duration (hour)	N (wt%)	H_2O (wt%)	C (wt%)	Type capsule	T (°C)	P (bar)	fH_2 (bar)	External sensor
A RUN 1	AR1FeN	B+Fe3,5N	1	0.67	-	-	AuPd	1200	800	10	CoPd
	AR1HNO3C	B+HNO3+G	1	1.44	3.5	10.0	AuPd	1200	800	10	CoPd
	AR1NH3	B+NH3	1	3.45	6.5	-	AuPd	1200	800	10	CoPd
A RUN 3	AR3FeNFeS	B+Fe3,5N+FeS	1	0.33	-	-	Pt	1200	800	5	NiPd
	AR3HNO3C	B+HNO3+G	1	1.44	3.5	7.0	AuPd	1200	800	5	NiPd
	AR3HNO3AgCO	B+HNO3+Ag2CO4	1	1.44	3.5	0.0	AuPd	1200	800	5	NiPd
A RUN 4	AR4NH3FeSClr	B+NH3+FeS+G+Ir	1	3.45	6.5	7.0	Pt	1200	2400	24	CoPd
	AR4HNO3CPd	B+HNO3+G+Pd	1	1.44	3.5	7.0	AuPd	1200	2400	24	CoPd
A RUN 5	AR5SiNFeN	B+Si3N4+Fe3,5N	1	1.78	-	-	AuPd	1300	900	10	CoPd
	AR5SiNFeNx2	B+Si3N4+Fe3,5N	1	3.56	-	-	AuPd	1300	900	10	CoPd
PC RUN 2	PCR2SiNFeN	B+Si3N4+Fe3,5N	1	1.78	-	-	Pt	1300	10000	-	-
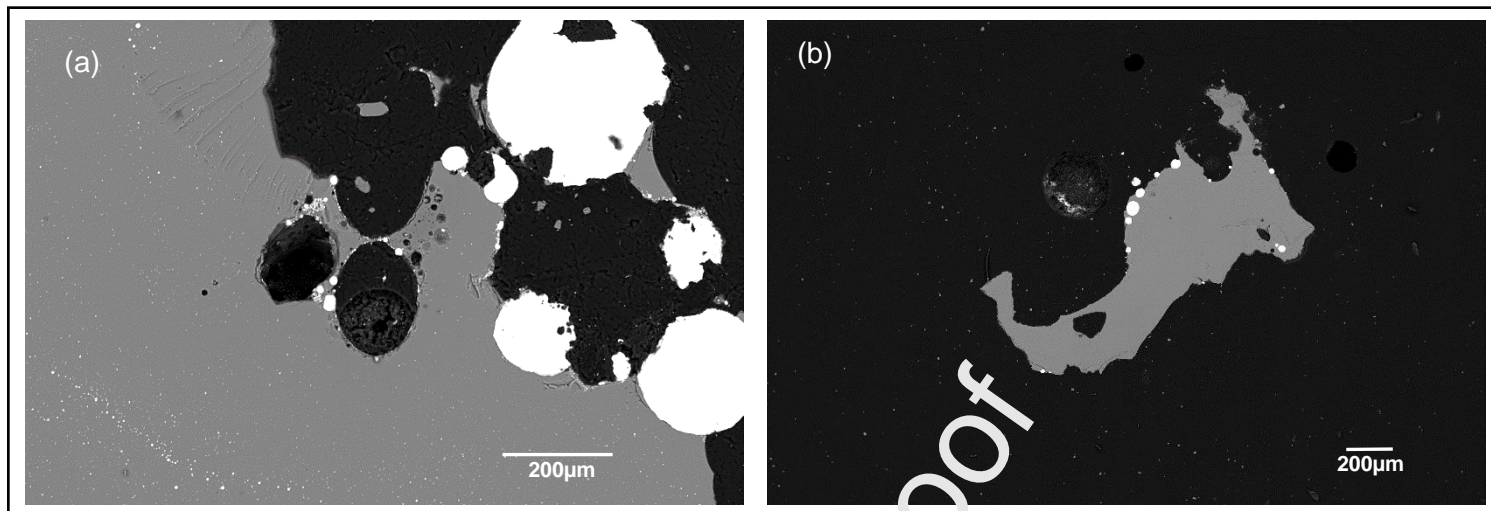
Figure. 1. Back scattered electron image (BSE) of (a) a part of the sample AR5SiNFeNx2 (Mag x177) with metal (white) and bubbles in the silicate glass (grey). (b) A part of the sample AR5SiNFeN (Mag x35) with metal droplets in silicate glass and bubbles. For the most reduced sample (AR5SiNFeNx2) with fO_2 IW-3.5 the formation of micronuggets was observed (a).

Table 2. Chemical compositions (wt%) silicate glasses and alloys determined by EPMA.

	AR1HNO$_3$C	1-σ	AR4NH$_3$FeSClr	1-σ	AR4HNO$_3$CPd	1-σ
SiO$_2$	48,36	0,09	45,99	0,26	47,13	1,02
TiO$_2$	1,67	0,12	1,46	0,13	1,40	0,12
Al$_2$O$_3$	14,70	0,12	14,28	0,09	13,49	0,24
FeO	6,40	0,43	7,48	0,16	8,23	0,23
MnO	0,15	0,02	0,14	0,07	0,12	0,05
MgO	8,37	0,13	8,55	0,05	8,24	0,11
CaO	12,57	0,28	11,12	0,16	10,82	0,18
Na$_2$O	3,49	0,12	3,18	0,03	3,21	0,12
K$_2$O	1,22	0,08	1,25	0,08	1,31	0,06
Total	96,91	0,40	94,08	0,41	93,97	0,70

	AR1HNO$_3$C	1-σ	AR4NH$_3$FeSClr	1-σ	AR4HNO$_3$CPd	1-σ
Si	0,53	0,57	0.01	0.0(	0.52	0.54
P	-	-	-	-	0.01	0.01
S	-	-	1.38	ͻ 7ͻ	0.00	0.00
Fe	22,29	0,35	3.52	1 ͻ4	10.53	0.21
Pd	77,02	1,94	0.00	0.ͻ0	84.66	2.05
Pt	-	-	0.00	0.00	0.22	0.32
Ir	-	-	84 5ͻ	5.14	-	-
Total	99,85	1,54	89.ͻ7	3.37	95.94	1.97

	AR5SiNFeN	1-σ	AR5SiNFeNx2	1-σ	PCR2SiNFeN	1-σ
SiO$_2$	52,99	0,85	ͻ6,71	0,76	54,85	0,38
TiO$_2$	1,49	0,07	0,79	0,20	1,44	0,05
Al$_2$O$_3$	14,80	0,2ͻ	14,96	0,21	14,83	0,15
FeO	2,66	ͻ,62	0,46	0,15	1,61	0,35
MnO	0,16	ͻ,05	0,18	0,05	0,18	0,07
MgO	9,11	ͻ,16	9,19	0,27	9,17	0,14
CaO	11,85	0,23	11,90	0,27	11,84	0,19
Na$_2$O	3,31	0,22	3,31	0,10	3,41	0,09
K$_2$O	1,30	0,08	1,29	0,09	1,32	0,04
Total	97,88	0,58	98,82	0,63	98,84	0,57

	AR5SiNFeN	1-σ	AR5SiNFeNx2	1-σ	PCR2SiNFeN	1-σ
Si	0.01	0.01	0,01	0,01	0,01	0,01
P	3.85	1.83	3,09	1,95	6,04	3,96
S	0.01	0.01	0,01	0,01	0,01	0,01
Fe	91.06	1.77	91,39	1,58	90,08	2,83
Pd	0.01	0.02	0,01	0,01	0,00	0,00
Pt	0.00	0.00	0,00	0,00	0,00	0,00
Ir	-	-	-	-	-	-
Total	94.95	0.45	94,51	0,67	96,15	1,23

	AR1FeN	1-σ	AR1NH₃C	1-σ	AR3HNO₃AgCO	1-σ
SiO$_2$	48,15	0,38	47.33	0.81	45,86	0,50
TiO$_2$	1,64	0,10	1.59	0.14	1,36	0,10
Al$_2$O$_3$	14,67	0,19	15.11	0.33	13,81	0,10
FeO	6,12	0,24	5.68	1.16	9,23	0,25
MnO	0,16	0,04	0.23	0.03	0,09	0,06
MgO	8,39	0,08	7.66	0.10	8,46	0,03
CaO	11,62	0,08	12.44	0.22	10,75	0,18
Na$_2$O	3,76	0,04	3.83	0.21	3,31	0,09
K$_2$O	1,37	0,04	1.22	0.11	1,27	0,08
Total	95,87	0,62	95.10	0.35	94,15	0,68

	AR3FeNFeS	1-σ	AR3HNO₃C	1-σ
SiO$_2$	48.36	0.19	46,79	0,21
TiO$_2$	1.42	0.15	1,53	0,09
Al$_2$O$_3$	15.48	0.09	14,08	0.1'
FeO	9.27	0.41	9,00	0,21
MnO	0.18	0.08	0,20	0,09
MgO	6.66	0.09	8,73	0,17
CaO	11.47	0.11	11,26	0,19
Na$_2$O	3.53	0.06	3,34	0,07
K$_2$O	1.43	0.05	1,2	0,07
Total	97.80	0.43	9.13	0,30

Table 3. Volatile concentrations in the silicate melt as a function of fO_2 (ΔIW).
(1) Description of the run product, G=Glass, Bbl=Bubble, Cr=Crystals, A=Alloy, C= Graphite

| Run	Name	log fO_2 (ΔIW)	N glass (ppm)	Err	H_2O (wt%)	Err	CO_2 (wt%)	Err	Run product description (1)
A RUN 1	AR1FeN	1.59	20.86	4.23	0.62	0.08	-	-	G+Bbl+Cr
	AR1HNO3C	2.18	9.27	2.80	0.42	0.02	-	-	G+Bbl+Cr+A+C
	AR1NH3	3.10	3.62	1.88	1.69	0.09	-	-	G+Bbl
A RUN 3	AR3FeNFeS	3.71	20.08	4.08	1.01	0.03	-	-	G+Bbl
	AR3HNO3C	4.21	7.04	2.13	1.44	0.06	0.01	0.0028	G+Bbl+C
	AR3HNO3AgCO	4.91	3.94	2.04	2.32	0.05	-	-	G+Bbl
A RUN 4	AR4NH3FeSClr	2.41	17.49	3.57	1.69	0.06	0.02	-	G+Bbl+A+S+C
	AR4HNO3CPd	3.08	26.26	5.33	2.76	0.06	0.08	0.0096	G+Bbl+A+C
A RUN 5	AR5SiNFeN	-2.94	93	3	0.04	0.02	-	-	G+Bbl+A
	AR5SiNFeNx2	-4.72	1737	112	0.02	0.01	-	-	G+Bbl+A
PC RUN 2	PCR2SiNFeN	-2.95	1504	34	0.05	0.01	-	-	G+Bbl+A

Table 4. The calculated fluid mixture in equilibrium with the different samples during the

RUN	Name	Pressure (bar)	fH$_2$O	Err	fCO$_2$	Err	fCO	fH$_2$	fN$_2$
A RUN 1	AR1FeN	800	49	6	-	-	-	10	741
A RUN 1	AR1HNO3C	800	97	4	-	-	-	10	693
A RUN 1	AR1Li&K	800	278	15	-	-	-	10	512
A RUN 3	AR3FeNFeS	800	112	2	-	-	-	5	683
A RUN 3	AR3HNO3C	800	200	8	300	71	0.25	5	295
A RUN 3	AR3HNO3AgCO	800	448	10	-	-	-	5	347
A RUN 4	AR4NH3FeSClr	2400	300	10	305	116	0.03	24	1771
A RUN 4	AR4HNO3CPd	2400	732	21.6	504	59.2	0.01	24	1140
A RUN 5	AR5SiNFeN	900	1	0.4	-	-	-	9	890
A RUN 5	AR5SiNFeNx2	900	0	0.03	-	-	-	9	891
PC RUN 2	PCR2SiNFeN	10000	-	-	-	-	-	-	56000

experiment.

Table 5. Comparison between the different calculated log fO2 (ΔIW). (1) Sensor calculation,(2) Fe-FeO calculation (equilibrium (6)), (3) H2-H2O calculation (equilibrium (9))

| Run	Name of sample	External log fO_2 [1]	Internal log fO_2 (FeO) [2]	Err	Internal log fO_2 (H_2O) [3]	Err
A Run 1	AR1FeN	3.39	-	-	1.59	0.12
A Run 1	AR1HNO3C		1.97	0.07	2.18	0.04
A Run 1	AR1Li&K		-	-	3.10	0.05
A Run 3	AR3FeNFeS		-	-	3.71	0.02
A Run 3	AR3HNO3C	4.40	-	-	4.21	0.04
A Run 3	AR3HNO3AgCO		-	-	4.91	0.02
A Run 4	AR4NH3FeSClr	3.80	2.47	0.09	2.41	0.03
A Run 4	AR4HNO3CPd		2.91	0.03	3.08	0.03
A Run 5	AR5SiNFeN	-	-2.53	0.20	-2.94	0.37
A Run 5	AR5SiNFeNx2		-4.50	0.?8	-4.72	0.43
PC Run 2	PCR2SiNFeN	-	-2.95	?.1?	-	-
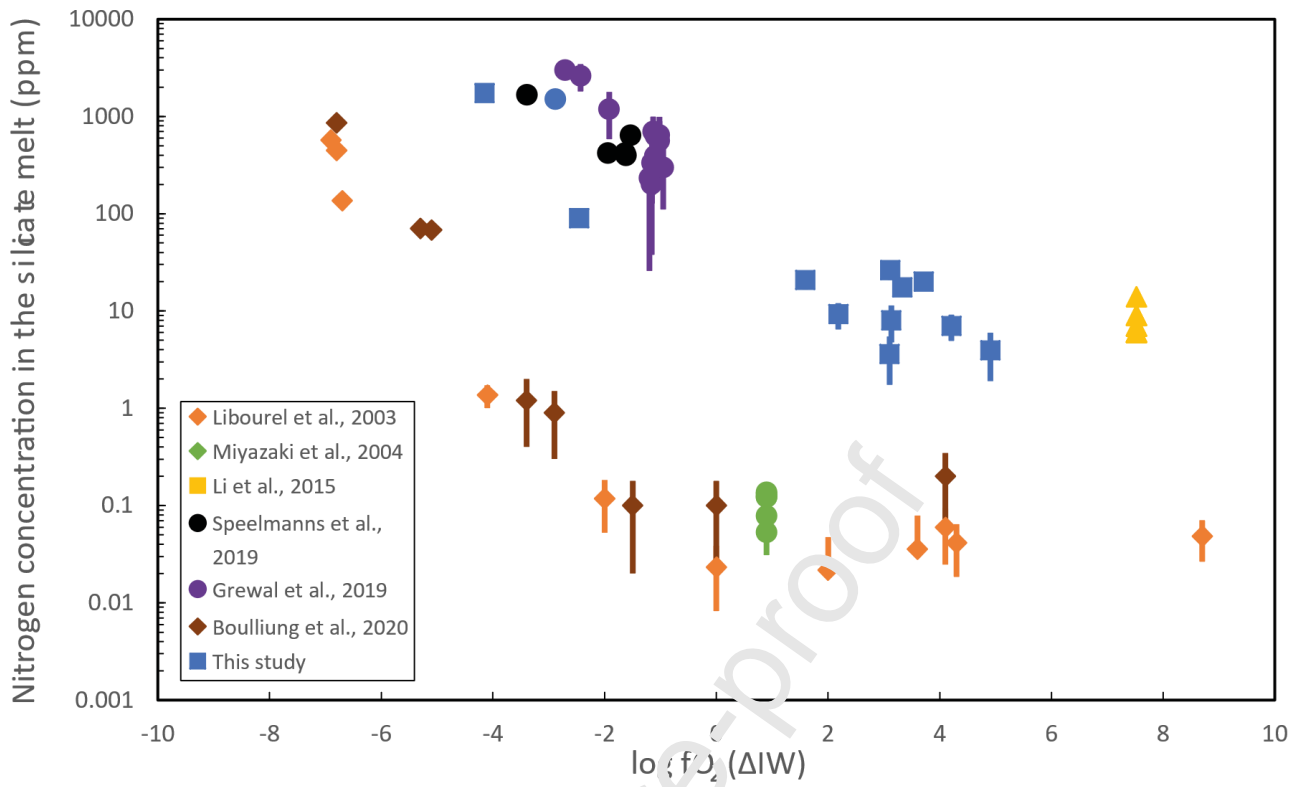
Figure. 2. Nitrogen concentration in basaltic silicate melt as a function of the fO$_2$ (ΔIW). Comparison of our experimental result (800 [blue square] to 10000 bar [blue circle]) with result of low-pressure study (ie. Libourel et al. 2003, Miyazaki et al. 2004, Boulliung et al. 2020; 1 bar) and high pressure study (ie. Grewal et al. 2019, Speelmanns et al. 2019 >10000 bar)
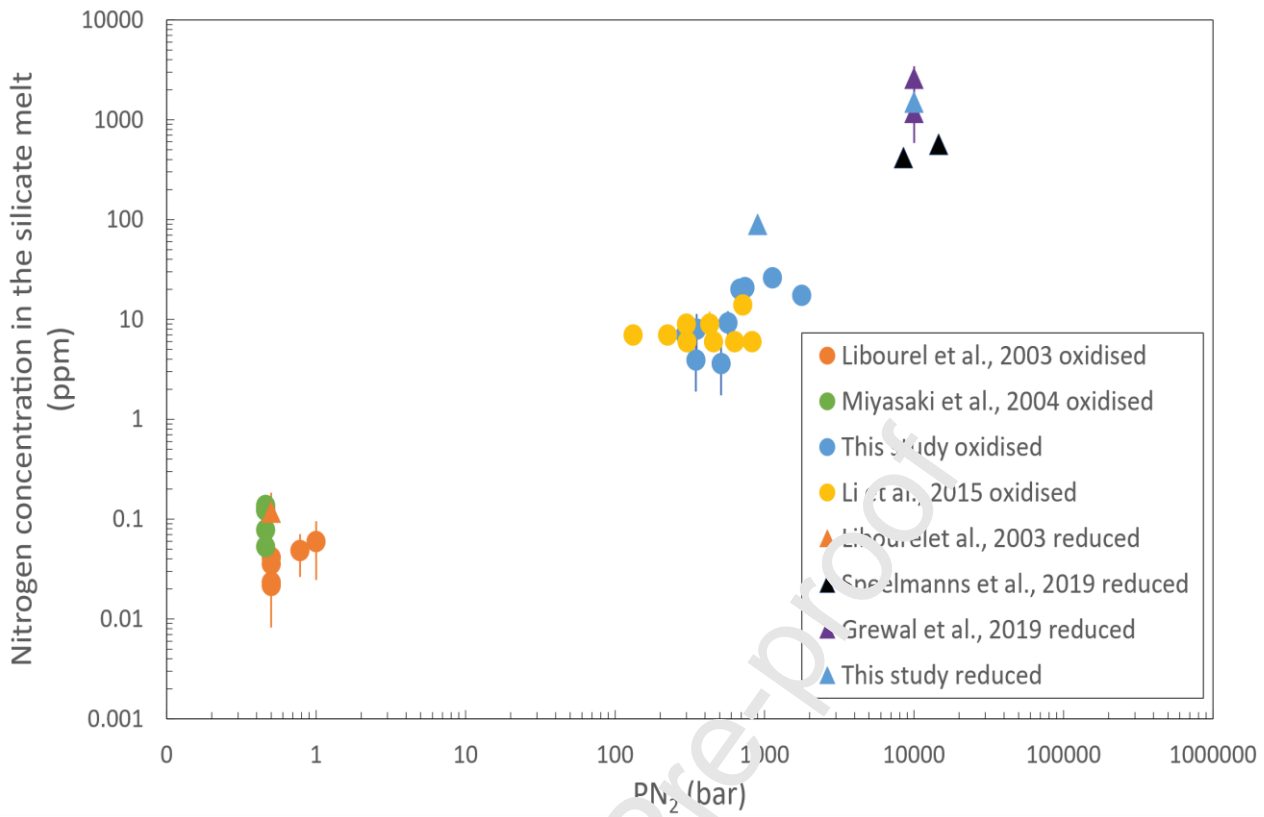
Figure. 3. Nitrogen concentration as a function of the nitrogen pressure. Result of oxidised experiments (log fO$_2$>IW) are shown, where the effect of the pressure is the clearest due to the limited impact of the fO$_2$. For more reduced conditions than IW, we select only data at log fO$_2$≈IW-2 in order to limit the strong effect of the fO$_2$ and identify the real impact of the P(N$_2$).

Table 6. Thermodynamic constants of the model adjusted with the database

| ΔH_{13} (J.mol^{-1})	ΔS_{13} (J.K.mol^{-1})	ΔV_{13} (J/bar)	ΔH_{14} (J.mol^{-1})	ΔS_{14} (J.K.mol^{-1})	ΔV_{14} (J/bar)
29344^{+5868}_{-7336}	-121^{+4}_{-6}	$4^{+0.6}_{-0.9}$	183733^{+551}_{-919}	$-172^{+0.2}_{-0.2}$	$-5^{+0.25}_{-0.06}$
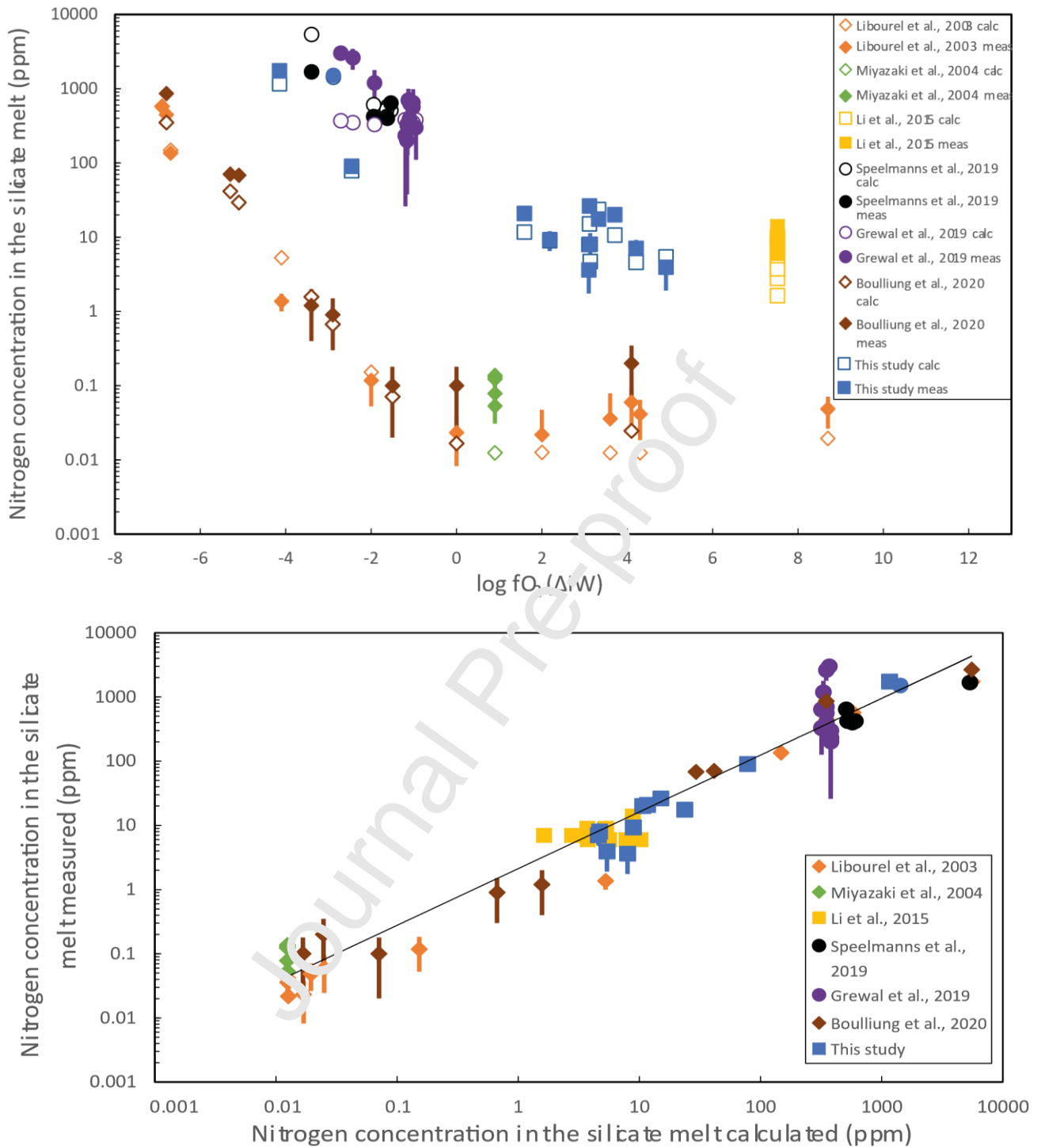
Figure. 4. Top diagram shows the difference between the measured nitrogen concentrations from different studies (full symbols) with the nitrogen concentration calculated by the model for identical conditions (open symbols) as a function of fO₂. Second diagram at the bottom is a plot of measured versus calculated nitrogen concentration in the silicate melt. These two diagrams highlight the reproducibility of the data obtained experimentally by the model for identical conditions.
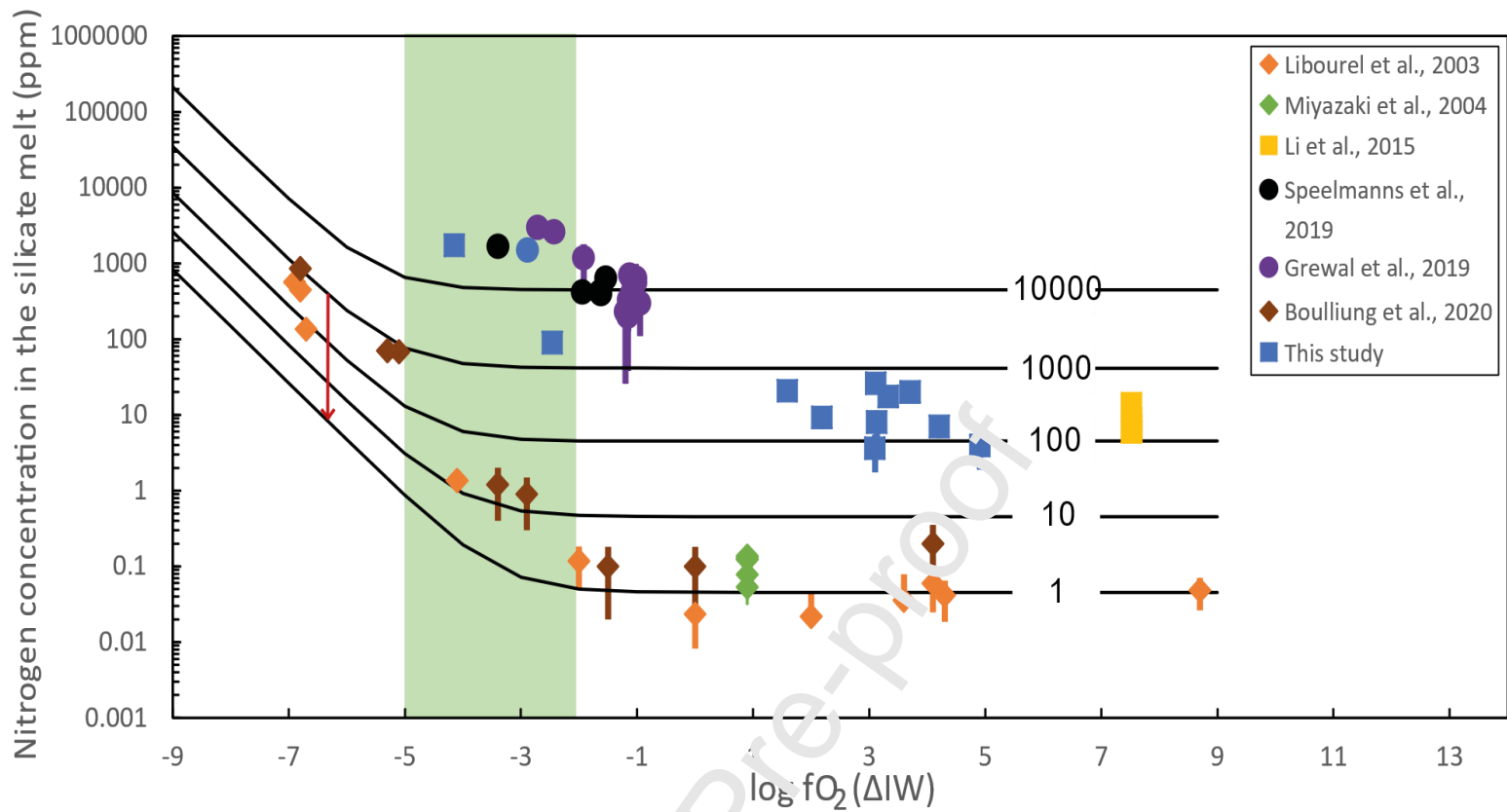
Figure. 5. Nitrogen fugacity isobars (bar) report on a nitrogen concentration diagram as a function oxygen fugacity. Use of isobars allow to check how the nitrogen solubility in basaltic silicate melt vary with the pressure combine to the oxygen fugacity. All the data use in this study was report. Green rectangle represents the interval of magma ocean redox conditions. Red arrow corresponds to the volcanic degassing scenario of mercury discuss in 4.4.

Declaration of interests

☒ The authors declare that they have no known competing financial interests or personal

relationships that could have appeared to influence the work reported in this paper.

☐The authors declare the following financial interests/personal relationships which may be considered as potential competing interests: